MRI-Guided Robot-Assisted Lumpectomy for Surgical Management of Early Breast Cancer: Preliminary Investigation and Use Case Analysis

Y. Yu, K. Yan, T. Podder, W.S. Ng, K. Brill, L. Liao

***Abstract*—Dynamic contrast enhanced magnetic resonance imaging (DCE MRI) in combination with ultrasound and/or x-ray imaging offers an excellent roadmap for intraoperative surgical guidance for complete excision of the true extent of disease in early stage breast cancer. However, incorporation of image-guidance in the operating room is challenging due to patient positioning, precise targeting under tissue deformation, instrument incompatibility and limited maneuverability, and complex human-technology interface. In this paper, we outline a novel strategy and preliminary simulation data on a proposed robot-assisted lumpectomy technique in the prone position using DCE MRI for real-time guidance. Extension to CT guidance for x-ray enhancing lesions would require minimal additional specifications. For ultrasound enhancing lesions, a method to ensure co-registration of the target with MRI is presented.**

I. Introduction

Advances in image-guided needle biopsies and imaging studies for disease mapping in breast cancer have evolved rapidly in the past decade. These include stereotactic large core biopsy under pneumatic assistance, dynamic contrast enhanced magnetic resonance imaging (DCE MRI), three-dimensional (3D) ultrasound, conebeam CT, and digital tomosynthesis. Investigational imaging techniques such as diffuse optical tomography [1] sono-contrast spectroscopy [2], ultrasound modulated optical tomography [3] and ultrasound tissue typing [4] are continually broadening the landscape of imaging-guided intervention and disease characterization in breast cancer.

In contrast, image-guided surgery for breast cancer mostly remains to be a less integrated and sometimes disparate set of workflows. In lumpectomy, the surgery is guided by localization wires placed in a separate, preoperative procedure performed by breast radiologist under conventional image guidance. Large variability exists in the amount of tissue excised around the wire, which often depends on surgeon preference (Fig. 1). Positive margin would occur if the excision is overly conservative compared to the true extent of the disease, and would be detected only after surgical pathology examination.

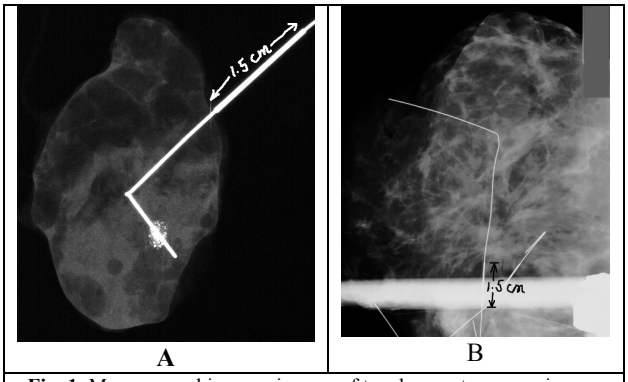

Fig. 1. Mammographic x-ray images of two lumpectomy specimens. (Note different scales.) These unselected specimens were sequentially received in the same day from different surgical services.

The root cause of this problem is that imaging and surgery have different operating requirements for positioning, immobilization, access, and time constraints.

Image-guided ablation techniques have been an area of active investigation as an attempt to address the problem identified above. Many investigators including our group have developed methods to deliver ablative energy such as radiofrequency (RF) and high intensity focused ultrasound (HIFU) to imaging defined lesions so as to achieve targeted cell death, sometimes without the need for invasive procedures [5,6]. It is notable that such ablative therapies are conceptually similar to radiation therapy, where a tumoricidal dose is precisely delivered to a targeted area. However, surgery (i.e. lumpectomy) remains to be the first line treatment, and surgical margin status continues to be an important parameter in the subsequent care of the patient, including chemotherapy, radiation therapy, and long term surveillance. Histopathology of the surgical specimen provides important information for the ongoing care of the patient. In these respects, development of a real-time image-guided lumpectomy technique is especially pertinent in the current clinical setting.

Minimally invasive surgical interventions under robotic assistance have achieved remarkable success of clinical adoption in prostatectomy and rapid development in prostate biopsy and brachytherapy [7,8]. We have previously demonstrated that interventional techniques currently used in

Corresponding author: Yan Yu (phone: 215-955-5998, e-mail: Yan.Yu@Jefferson.edu)

Y. Yu, K. Yan, Y. Podder: Department of Radiation Oncology, Jefferson Medical College, Thomas Jefferson University, Philadelphia, PA 19107 USA

W.S. Ng: School of Mechanical and Aerospace Engineering, Nanyang Technological University, Singapore.

K. Brill: Department of Surgery, Jefferson Medical College, Thomas Jefferson University, Philadelphia, PA 19107 USA

L. Liao: Cooper Cancer Institute and Department of Radiology, Robert Wood Johnson University, Voorhees, NJ 08403 USA

breast cancer can be guided by a similarly optimized robotic system to achieve higher positions of targeted tissue retrieval [9]. Ongoing research efforts in biomedical applications of MEMS technology promise to further expand the capabilities of real-time clinician-directed steering mechanisms. Online control strategies for optimal steering of flexible interstitial probe/needles have concurrently been developed with the ultimate goal of opening up a curvilinear space of interstitial surgical access [10-13]. This body of recent investigations provides a platform of enabling technologies for achieving percutaneous, minimally invasive lumpectomy under real-time image-guidance and robotic assistance.

In this paper, we outline a design framework for bioinformatics-driven workflow in the proposed paradigm of percutaneous lumpectomy.

II. FLEXIBLE INSTRUMENT CONTROL/STEERING STRATEGY

A. The dynamic equations of flexible instrument-tissue interaction model

According to the study in [14], most living tissues have viscoelastic behaviors, as long as small displacements are considered. Here in this study, a continuously distributed Kelvin Voigt (KV) model [11] that consists of equivalent spring and viscous (damper) elements is considered to model the tissue reaction forces during instrument steering procedure. The flexible instrument is assumed to follow the Bernoulli-Euler beam model that mainly considers the instrument deflection caused by bending instead of shearing [16]. The steering force will be applied at the base of the instrument. During the steering procedure, not only the tissue deformation and the flexibility of the instrument, but also their interaction should be taken into consideration. The system dynamic equation can be derived using Hamilton's principle as follows:

$$\int_{t_1}^{t_2} (\delta T - \delta V + \delta W_{nc}) dt = 0 \qquad (1)$$

T: kinetic energy
V: potential energy
W_{nc} : work done by non-conservative forces

To facilitate the modeling procedure, a local coordinate system ($\tilde{x}$ - $\tilde{y}$) that is attached at the base of the instrument and moves with it is introduced using the Galilean transformation. The system kinetic energy, potential energy and virtual work done by all the non-conservative forces (steering force F_y and damping forces), are given by

$$T = \frac{1}{2} M \dot{y}^2 + \int_0^L \frac{1}{2} \rho (\dot{y}(t) + \dot{\omega}(\tilde{x}, t))^2 d\tilde{x} = T(\dot{y}, \dot{\omega}) \qquad (2)$$

$$V = \int_0^L \frac{1}{2} EI\omega''^2 d\tilde{x} + \int_0^L H(\tilde{x} - L + v_x t) \cdot \frac{1}{2} k[y(t) + \omega(\tilde{x}, t) - y(t + \frac{\tilde{x} - L}{v_x}) - \omega(L, \frac{\tilde{x} - L}{v_x} + t)]^2 d\tilde{x}$$
$$\xrightarrow{h(t) = L - v_x t} \int_0^L \frac{1}{2} EI\omega''^2 d\tilde{x} + \int_0^L H(\tilde{x} - h(t)) \cdot \frac{1}{2} k[y(t) + \omega(\tilde{x}, t) - y(\frac{\tilde{x} - h(t)}{v_x}) - \omega(L, \frac{\tilde{x} - h(t)}{v_x})]^2 d\tilde{x} \qquad (3)$$

$$H(x) = \begin{cases} 1 \ldots x \geq 0 \\ 0 \ldots x < 0 \end{cases} \qquad (4)$$

$$\delta W_{nc} = F_y \cdot \delta y - \int_0^L H(\tilde{x} - L + v_x t) \cdot c(\dot{y} + \dot{\omega}) \cdot \delta(y + \omega) d\tilde{x} \qquad (5)$$

Here, v_x is needle insertion velocity, which is assumed to be constant for modeling simplicity. $h(t) = L - v_x t$ is the position of the insertion point in the moving coordinates system at time instant t. M is the mass of the fixture, which links the instrument with the 3D motion platform; L is the length of the elastic beam; ρ is the mass per unit length of the elastic beam; E is the Young's modulus of the instrument; I is the second moment of inertial about the z axis. k is the stiffness coefficient of the spring per unit length, and c is the damper coefficient per unit length. y is the base position in y axis; $\dot{y}(t)$ is the corresponding velocity at time instant t. ω is the deflection of the beam along the body at time instance t. $\dot{\omega}$ and ω'' are the first and second derivatives of the beam deflection with respect to time and space, respectively.

Unconstrained modal analysis was used to solve the dynamic equations. After some algebraic manipulations (refer to [11] for more details), the model can finally be derived as bellow.

$$M_t \ddot{\alpha}(t) + c v_x \dot{\alpha}(t) t + \sum_j^n \dot{q}_j(t) c \boxed{\int_{L - v_x t}^{L} \varphi_j(\tilde{x}) d\tilde{x}} + \sum_j^n q_j(t) k \boxed{\int_{L - v_x t}^{L} \varphi_j(\tilde{x}) d\tilde{x}} + k v_x \alpha(t) t = F_y + f_2 \qquad (6)$$

$$\dot{\alpha}(t) c \boxed{\int_{L - v_x t}^{L} \varphi_i(\tilde{x}) d\tilde{x}} + \alpha(t) k \boxed{\int_{L - v_x t}^{L} \varphi_i(\tilde{x}) d\tilde{x}} + \ddot{q}_i(t) + \sum_j^n \dot{q}_j(t) c \boxed{\int_{L - v_x t}^{L} \varphi_i(\tilde{x}) \varphi_j(\tilde{x}) d\tilde{x}} + \sum_j^n q_j(t) k \boxed{\int_{L - v_x t}^{L} \varphi_i(\tilde{x}) \varphi_j(\tilde{x}) d\tilde{x}} + \xi_i^2 q_i(t) = F_y \beta_i + f_{1i} \qquad (7)$$

where,

$$f_{1i} = \int_0^t k\alpha(t_1) \varphi_i(v_x t_1 + L - v_x t) v_x dt_1 + \int_0^t k \sum_j^n \varphi_j(L) q_j(t_1) \varphi_i(v_x t_1 + L - v_x t) v_x dt_1$$
$$= \int_0^t k y_T(t_1) \varphi_i(v_x t_1 + L - v_x t) v_x dt_1$$

$$f_2 = \int_0^t k\alpha(t_1) v_x dt_1 + \int_0^t k \sum_j^n \varphi_j(L) q_j(t_1) v_x dt_1 = \int_0^t k y_T(t_1) v_x dt_1$$

here, M_t is the total mass of the fixture and instrument , $y_T(t_1) = \alpha(t) + \sum_{i=1}^{n} \varphi_i(L) q_i$ is the tip position at time instant t_1. F_y is the lateral steering force, which is acted at the base in y direction. α(t) describes the motion of the center of mass of the total system without perturbation, $q(t)$ is the time-varying amplitude of motion that is the time solution of the deflection. β is defined to satisfy $\beta = -\frac{\rho}{M_t} \int_0^L \phi(\tilde{x}) d\tilde{x}$, where $\phi(\tilde{x})$ is the shape function. $\varphi(\tilde{x})$ is defined to be $\varphi(\tilde{x}) \equiv \beta + \phi(\tilde{x})$.

These partial differential equations can be solved using

Explicit Runge-Kutta (4,5) formula, the Dormand-Prince pair. A Matlab simulation program has been developed to simulate this model. With the applied needle base force F_y that is the input of the model, α and q_i will change with time, thus causing the changing of the needle tip position, as well as the tissue reaction forces. The only computational costly parts are the space-varying integrals, $\int_{L-v_x t}^{L} \varphi_j(\tilde{x})d\tilde{x}$ and $\int_{L-v_x t}^{L} \varphi_i(\tilde{x})\varphi_j(\tilde{x})d\tilde{x}$ highlighted in box in Equations (6) and (7), but they can be pre-computed once for all by choosing a small sample depth. The whole simulation will just take for a few minutes.

B. Adaptive Flexible Instrument Steering System

Considering the unknown, depth varying spring and damper coefficients resulted from tissue inhomogeneity and possible tissue variations between patients, adaptive control can be used for the design of the steering system. An adaptive controller is formed by combining an online parameter estimator, which provides estimates of the unknown parameters at each time instant, with a control law that is motivated from the known parameter case. There are two schemes for the adjustment: direct scheme and indirect scheme. The advantage of using the direct structure is potentially more efficient in the implementation as the design block can be rather computationally demanding. However not all control algorithms can be parameterized for use in the direct structure. In comparison, the indirect structure is more flexible in implementing different controller algorithms and is considered as a potential choice for the design of the steering system.

The indirect adaptive control system, in which the plant parameters are estimated online and used to calculate the controller parameters, can be illustrated using the following block diagram. The design of the online parameter estimator is presented in the next section.

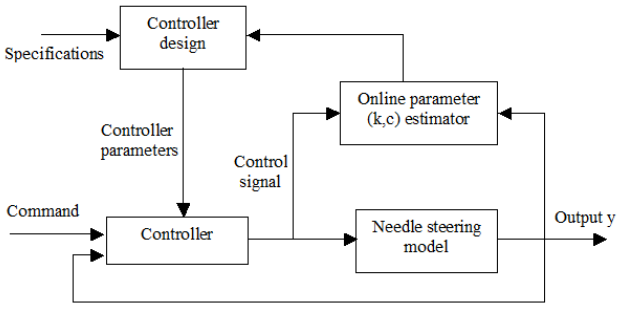

Fig. 2. Diagram of indirect adaptive control system

C. Online parameter estimator using modified least square with forgetting factor

Modified least square method with forgetting factor is used here for the design of the online parameter estimator. The issue here is to determine the parameter vector $\hat{\theta} = [k \quad c]^T$ in such a way that the outputs computed from the system model agree as closely as possible with the system output measurements in the sense of least squares, where $\hat{\theta}$ is the estimate of θ. The parameter vector $\hat{\theta}$ should be chosen to minimize the least-square minimization criterion

$$\begin{aligned} V(\hat{\theta}, n) &= \frac{1}{2}\sum_{k=1}^{n} \lambda(\vec{Y}_k - \hat{\vec{Y}}_k)^2 \\ &= \frac{1}{2}\sum_{k=1}^{n} \lambda(\vec{Y}_k - \mathrm{X}_{k-1}^T \hat{\theta})^2 \end{aligned} \tag{8}$$

that is, $\hat{\theta} = \arg\min_A V(\theta)$. λ is the forgetting factor.

Thus, the modified least-square estimation with covariance resetting and forgetting factor takes the form [15]:

$$\begin{aligned} \theta_k &= \theta_{k-1} + K_k(\vec{Y}_k - \mathrm{X}_{k-1}^T \hat{\theta}_{k-1}) \\ K_k &= P_{k-1}X_{k-1}[\lambda I + \mathrm{X}_{k-1}^T P_{k-1} X_{k-1}]^{-1} \\ P_k &= [P_{k-1} - K_k \mathrm{X}_{k-1}^T P_{k-1}]/\lambda \end{aligned} \tag{9}$$

where P_k and K_k are the computed covariance matrix and gain respectively at step *k*.

III. PRELIMINARY EXPERIMENTS ON MODEL VALIDATION

A. *Material and method*

Preliminary experiments were carried out first to validate the steering model before designing the controller based on this model. The experimental setup shown in Fig. 2 is used to carry out the experiment. The 3 Degree-of-Freedom (DOF) motion platform can drive the needle to follow some pre-determined trajectories. A 6 DOF force/torque (F/T) sensor (Nano17-SI-12-0.12, ATI Industrial Automation, USA) is mounted at the needle base to measure the needle base force. The needle used here is a 5-DOF MagTrax Needle Probe (Traxtal Technology, Canada). It is 130mm in length, has a trihedral tip, and a 19G stylet with 18G cannula. It has two sensors located at the stylet's distal tip and base respectively. The movement of the two needle points can be observed in real time via an electromagnetic system (Aurora, Northern Digital Inc. Canada). The gelatin phantom molded from gelatin and water were used to simulate the soft tissue. Considering tissue inhomogeneity, different stiffness PVC lumps, undissolved gelatin lumps and bubbles were added into the gelatin solution to make an inhomogeneous phantom, as shown in Fig. 3.

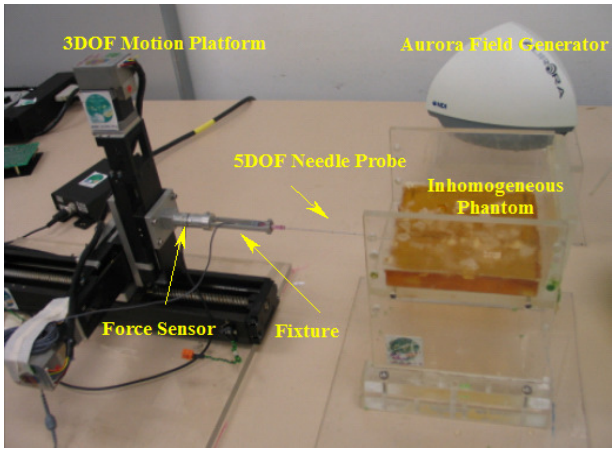

Fig. 3. Experimental setup

An 'active' way of validating the proposed model by steering the needle tip to a defined position will require a steering strategy that falls within a future scope of investigation. Instead, a 'passive' way of validation has been used to show that the model can accurately predict the needle tip trajectory when giving some inputs - needle base lateral forces. The procedure is illustrated below.

During the experiment, the needle was driven into the prepared phantom by the 3DOF platform following some pre-determined trajectories. The needle tip and base positions and corresponding needle base force data were collected during the procedure. These collected datasets were first passed through a filter designed using 50 moving average to remove the measurement noises and smooth the data. After that, the datasets went through the online parameter estimator to estimate the parameters ($\overline{k}_k, \overline{c}_k$). At the same time, the model was simulated using the online estimated parameters and the collected dataset ($y_k, y_{k-1}, \ldots$) to predict the output, the needle tip position (y_{k+1}). The simulated outputs, the needle tip position data, were compared with the measured position data during the experiments and the estimation errors went into the parameter estimator to adjust the estimations.

B. Simulation results and discussion

Since the tumor is normally embedded in certain depth inside the tissue, the needle was first inserted into the phantom following straight-line insertion before lateral movement was actuated. The total needle insertion depth was 8cm and lateral movement was 2cm starting at insertion depth of 4cm. The insertion speed was set to be 4mm/s. The lateral speed was chosen to be 2mm/s in order to keep the movements in x and y to start and stop simultaneously. The initial spring and damper coefficients were set to be 3×10^5 N/m^2 and 2×10^6 N.s/m^2 respectively. The initial covariance was set to be 10^{18} and the forgetting factor was selected to be 0.95. Figure 4 showed the estimation results. Even though at the beginning the error was large due to the initial estimation, it converged very fast and the accuracy was satisfactory. The RMS error after convergence is 0.121mm.

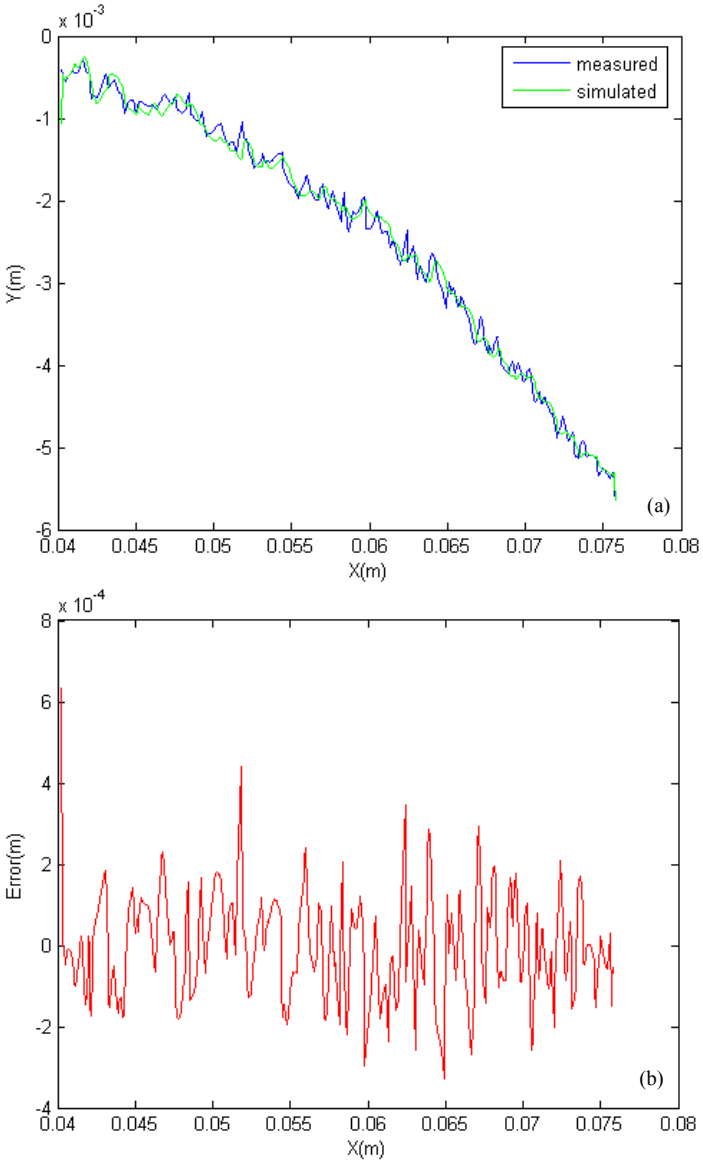

Fig.4. Inhomogeneous phantom with support: (a) Simulated vs. measured tip trajectory (b) Simulation errors

IV. USE CASE ANALYSIS

This section outlines our framework for DCE MRI-driven workflow in a novel paradigm of percutaneous lumpectomy in the surgical management of early stage breast cancer patients. This framework provides a roadmap towards implementing the key elements in image-guided, robot-assisted breast surgery.

A. Preoperative planning and simulation

The preoperative planning use case specifies the workflow requirements after tissue diagnosis of a breast cancer to the point before surgical setup of the patient. The suitable patient would have unifocal breast cancer with tumor size

less than 3 cm and have demonstrated strong MRI enhancement with Gadolinium. The most ideal location of the tumor is in the anterior and mid breast with at least 1 cm negative margin to the chest wall structures. Other contraindications of MRI guided lumpectomy are the same as well established contraindications for routine MRI studies published in the literature.

The patient will have undergone diagnostic imaging studies that include DCE MRI in combination with ultrasound and/or an x-ray modality (mammography, breast CT, digital tomosynthesis). The prone position is adopted for all 3D imaging modalities to achieve co-registration with DCE MRI; thus, identical positioning for other imaging modalities such as ultrasound and CT will be achieved using compatible support assemblies (Fig.5.). The target lesion, which can be enhancing in one or more modalities, is manually segmented in DCE MRI by reference to other imaging modalities using standard mutual information (MI) based image fusion. A desired excision margin as specified by the surgeon is calculated in 3D from the segmented contours. The 3D surgical target is thus defined by the breast imaging and surgical team preoperatively in relation to the patient anatomy and surgical approach. The preoperative planning module uses this information to construct a 3D environment, which also simulates the surgical tool trajectories necessary for complete removal of the target volume. The approach of needle advancement (medial-lateral or lateral-media) is determined based on the location of the lesion in the breast.

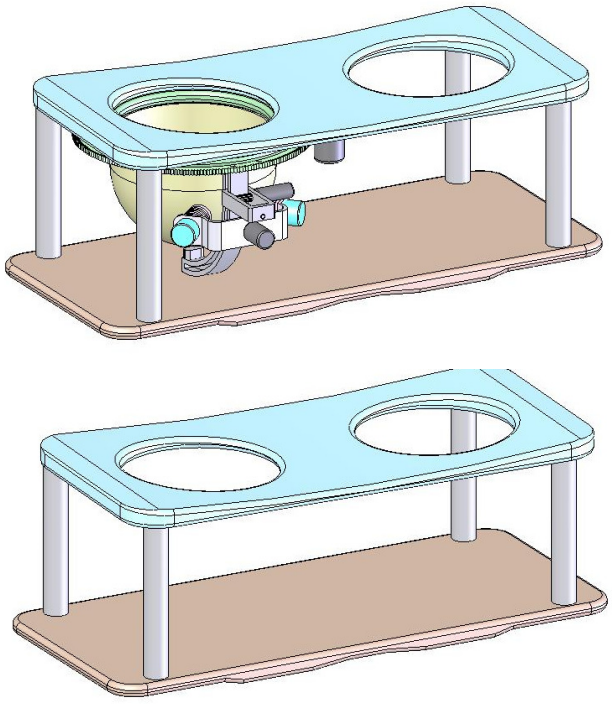

Fig. 5. Ultrasound and CT/PET imaging in the prone position: (top) Ultrasound volumetric scanning cup (degassed water interface); (bottom) Carbonfiber patient support device compatible with CT and PET imaging.

B. Intraoperative planning and surgical guidance

The intraoperative planning and surgical guidance use case specifies the workflow requirements from surgical setup of the patient to the completion of robotic lumpectomy. Similar to MRI-guided breast biopsy, the patient is set up in the prone position. The patient will be conscious-sedated prior to the procedure with monitoring system located outside the MRI field. The target breast is compressed gently by specialized MRI procedure compression plates containing embedded measurement grids and fiducials for robot space co-registration. A unilateral high resolution breast MRI with axial, sagittal T1 with fat suppression acquisitions will be obtained immediately prior to MRI procedure after 10 – 15 cc (weight dependent) of Gadolinium intravenous injection for confirmation of the tumor location and size. A 3D reconstruction and maximum intensity projection (MIP) module will also be obtained for mapping. This intraoperative planning scan is fused with the preoperative 3D image set, which co-registers the target volume and robotic planning and execution workspace. The MRI table is then moved out the scanner for procedure. The entrance point of the needle is marked on the breast. The depth of needle advancement is calculated. The area is prepared in usual surgical manner. A small incision is made (if needed) after adequate local anesthetization. The needle is manually advanced to the target. The table is then moved back to the scanner, and a second 10 – 15 cc of IV Gadolinium is given. A repeat axial and sagittal acquisition is obtained followed by 3D reconstruction and MIP to confirm that the needle is in the correct location. After 3D imaging confirmation, the table is again moved out of the MRI scanner and the lumpectomy procedure is performed under software visualization and robotic control assistance. At the completion of the procedure, the patient is scanned again with a third 10 – 15 cc IV contrast for evaluation of margins. Re-excision will be carried out immediately under robotic control and software visualization if inadequate excision is demonstrated by margin enhancement; otherwise if margin enhancement is negative, the procedure is considered complete.

Sentinel lymph node will be determined using the current standard technique of nuclear imaging. The location of the sentinel lymph node will be marked on the skin by a fat containing fiducial (Vitamin E capsule) prior to MRI study. The lymph node will be mapped in 3D fashion for concurrent MRI-guided procedure of tissue sampling. Tissue acquisition can adopt the established method in MRI-guided breast lesion biopsy. If other suspicious lymph nodes have been identified during MRI staging, a similar MRI-guide tissue acquisition method will be applied.

The MRI-guided lymph node tissue sampling step does not necessarily require contrast injection, and can be performed in the same setting as but after the completion of robotic lumpectomy.

Surgical excision specimen is identified by its relative location from the margin of the target lesion using software

visualization and robotic control. All excised specimens are evaluated by surgical pathology for histological status. If positive margin is identified, the patient will be offered conventional surgical re-excision.

V. CONCLUSION

A multi-modality image-guided lumpectomy methodology is outlined. It requires patient setup in the prone position compatible with DCE MRI. Lesions that enhance under ultrasound or other imaging modalities are co-registered to MRI by imaging the patient in the same prone position via a set of specifically designed support devices. Preoperative planning and surgical simulation are carried out in the MRI image space. Surgical excision is performed under robotic assistance and steerable end-effecter control strategy in the MRI suite within a set of dynamic contrast enhancement protocols. Lymph node dissection is similarly performed under MRI guidance. Substantial future work is needed to demonstrate clinical feasibility of this methodology.

REFERENCES

[1] L.C. Enfield, A.P. Gibson, N.L. Everdell, D.T. Delpy, M. Schweiger , S.R. Arridge, C. Richardson, M. Keshtgar, M. Douek, J.C. Three-dimensional time-resolved optical mammography of the uncompressed breast. Appl. Opt 2007 Jun 10; 46(17):3628-38.

[2] Y. Yu, Y. Hu, K. Yan, T. Podder, and L. Liao, "Sono-contrast spectroscopy for breast cancer detection", Optics in Health Care and Biomed Optics III, Proc. SPIE Vol 6826 68260F-1 – 7, 2007.

[3] J. Li and L. V. Wang, Ultrasound-modulated optical computed tomography of biological tissues, Appl. Phys. Lett., 2004, 84(9), 1597-1599.

[4] T. Liu, F.L Lizzi,, J.A.Ketterling, R. H. Silverman, and G.J. Kutcher, , "Ultrasonic tissue characterization via 2-D spectrum analysis: theory and in vitro measurements," Med Phys, 2007 March:34(3):1037-1046, 2007.

[5] H.I. Vargas, W.C. Dooley, R.A. Gardner, K.D. Gonzalez, R. Venegas , S.H. Heywang-Kobrunner, AJ Fenn. Focused microwave phased array thermotherapy for ablation of early-stage breast cancer: results of thermal dose escalation. Ann Surg Oncol. 2004, 11:139-46.

[6] Y. Hu, T. Podder, K. Yan, L. Liao, K. Parker, Yan Yu, "Tissue Ablation by Medium Intensity Focused Ultrasound for Breast Cancer Treatment: Preliminary Study", Medical Physics, 35(6), 2639, June 2008.

[7] L. Phee, J. Yuen, D. Xiao, C. F. Chan, H. Ho, C. H. Thng, P. H. Tan, C. Cheng, W. S. Ng. Ultrasound Guided Robotic Biopsy of the Prostate. International Journal of Humanoid Robotics (IJHR), 2006 3(4), 463-483.

[8] Y. Yu , T. K.Podder, Y. D.Zhang, W. S.Ng, V. Misic, J.Sherman, D.Fuller, D. J.Rubens, J. G.Strang, R. A.Brasacchio and E.M.Messing, 'Robotic system for prostate brachytherapy', Computer Aided Surgery, 2007, 12:6, 366 – 375.

[9] T. K.Podder,, L.Liao, J. Sherman, V.Misic, Y.D. Zhang, D.Fuller, D.J.Rubens, E.M.Messing, J.G.Strang, W.S.Ng, Y.Yu, "Assessment of Prostate Brachytherapy and Breast Biopsy Needle Insertions and Methods to Improve Accuracy," in the Proceedings of the 12th IEEE International Conference on Biomedical Engineering (ICBME), Singapore, December 7-10, 2005.

[10] K. Yan, T. Podder, D. Xiao, Y.Yu, T.I. Liu, , K.K.,Ling, and W.S.Ng, Online parameter estimation for surgical needle steering model. In Medical Image Computing and Computer-Assisted Intervention - MICCAI 2006, Rasmus Larsen, Mads Nielsen, Jon Sporring, eds. Springer, LNCS41900041, vol. 4190, isbn 3-540-44707-5, 2006, p321-329.

[11] K. Yan, T. Podder, Y. Yu, T.-I Liu, C.W.S Cheng, W. S. Ng, "Flexible Needle-Tissue Interaction Modeling with Depth-varying Mean Parameter: Preliminary Study", IEEE Transaction of Biomedical Engineering, Digital Object Identifier: 10.1109/TBME.2007.896586,2007.

[12] V.G. Mallaparagada, N. Sarkar, and T.K. Podder, "A Robotic System for Real-time Tumor Manipulation During Image-guided Breast Biopsy," in the IEEE Int. Conf. on Bioinformatics and Biomedical Engineering (BIBE), pp. 204-210, October.

[13] V.G. Mallaparagada, N. Sarkar, and T.K. Podder, "Robot Assisted Real-time Tumor Manipulation for Breast Biopsy," in the IEEE International Conference on Robotics and Automation (ICRA), pp. 2515-2520, May 2008.

[14] Y. C. Fung. "Biomechanics: Mechanical Properties of Living Tissues", Springer-Verlag. ISBN: 0387979476, 1993.

[15] P. A.ioannou, J. Sun. "Robust Adaptive Control", PTR Prentice-Hall, Upper Saddle River, NJ 07458, 1996.

[16] C. Wit, B. Siciliano and G.Bastin (eds.) . "Theory of Robot Control", Springer,1996.